Ocean Engineering 78 (2014) 73–88

Contents lists available at ScienceDirect

Ocean Engineering

journal homepage: www.elsevier.com/locate/oceaneng

Numerical study on the water impact of 3D bodies by an explicit finite element method

Shan Wang, C. Guedes Soares *

Centre for Marine Technology and Engineering (CENTEC), Instituto Superior Técnico, University of Lisbon, Lisboa, Portugal

ARTICLE INFO

Article history:
Received 26 April 2013
Accepted 14 December 2013
Available online 31 January 2014

Keywords:
Numerical modeling
Water impact
Explicit finite element method
Impact coefficient
Slamming
Wave converter

ABSTRACT

The hydrodynamic problem of the water impact of three-dimensional buoys is investigated by the explicit finite element method with an Arbitrary-Lagrangian Eulerian (ALE) solver. The fluid is solved by using an Eulerian formulation, while the structure is discretized by a Lagrangian approach, and a penalty coupling algorithm enables the interaction between the body and the fluids. The remap step in the ALE algorithm applies a donor cell+HIS (Half-Index-Shift) advection algorithm to update fluid velocity and history variables. The interface between the solid structure and the fluids is captured by Volume of Fluid method. Convergence studies are carried out for three dimensional hemisphere and cones with different deadrise angles. It is found that the mesh density of the impact domain is very important to the quality of the simulation results. The contact stiffness between the coupling nodes affects the local peak pressure values. The numerical calculations are validated by comparing with other available results, for both the drop cases and the ones with constant impact velocity.

1. Introduction

Ocean waves are a significant resource of inexhaustible, non-polluting energy. Waves are caused by the wind blowing over the surface of the ocean. In many areas of the world, the wind blows with enough consistency and force to provide continuous waves. A variety of technologies have been proposed to capture the energy from waves, and they differ in their orientation to the waves with which they are interacting and in the manner in which they convert the energy of the waves into other energy forms. Wave energy converters provide a means of transforming wave energy into usable electrical energy.

Point absorbers are one type of wave energy converters that have small dimensions relative to the incident wave length. They can capture wave energy from a wave front that is larger than the dimensions of the absorber. Several types of wave absorbers have been proposed based on different mechanisms of obtaining relative motions between two bodies. Due to their relatively small size, the amount of energy that they can capture is relatively small as compared with devices based on other principles in Guedes Soares et al. (2012) and Silva et al. (2013). To overcome this limitation a possibility is having a large platform fixed or floating around which several small floaters have heaving type of motions, which can then be converted in power by the power take off mechanism in Vantorre et al. (2004), Lendenmann et al. (2007), Estefen et al. (2008) and Marquis et al. (2010). However, in this process it may happen that the floaters when at resonance have too high vertical displacements and will move out of the water, impacting it at the entrance. This problem has been detected by De Backer et al. (2008), who gives a brief introduction on how the power absorption is calculated, how the slamming restriction is formulated and fulfilled, and they found that there is a significant reduction in power absorption due to the slamming restriction. Since, in any case, the penalty to overcome slamming of the point absorbers completely will be too high and a certain level of slamming will usually be allowed, it is important to know the magnitude of the slamming load on the floating objects with different shapes.

De Backer et al. (2009), conducted an experimental study of the impact of 3D bodies during water entry, in order to assess the slamming loads in these buoys appropriate to the wave energy devices under consideration. This paper uses these experimental results as references to validate 3D numerical studies, which follow earlier work in 2D.

Early studies on the local slamming problem focused on the analysis of two-dimensional structures, since slamming on ships has been a major concern and the 2D strip theory has been widely used in ship motions research. The important pioneering study on this subject can be attributed to von Kármàn (1929) who proposed the first theoretical method on the analysis of seaplane landing. Then, Wagner (1932) developed an asymptotic solution for water entry of two-dimensional bodies with small local deadrise angles

* Corresponding author. Tel.: +351 218417957; fax: +351 218474015.
E-mail address: guedess@mar.ist.utl.pt (C. Guedes Soares).

0029-8018/$ - see front matter © 2013 Elsevier Ltd. All rights reserved.
http://dx.doi.org/10.1016/j.oceaneng.2013.12.008

by approximating them with a flat plate, which considered the local water surface elevation. For the idealized case of a wedge entering the calm water, Dobrovol'skaya, 1969 derived an analytical solution by transferring the potential flow problem for the constant water entry into a self similar flow problem in complex plane, which took advantage of the simplicity of the body geometry and is valid for any deadrise angle.

Zhao and Faltinsen (1993, 1996) proposed a nonlinear boundary element method to study the water entry of a two-dimensional body of arbitrary cross-section and generalized the Wagner (1932)'s theory to presented a simple asymptotic solution for small deadrise angles. As a further development work, a fully nonlinear numerical simulation method which includes flow separation from knuckles of a body was presented by Zhao et al., 1996. Sun and Faltinsen (2006) developed a two-dimensional boundary element method to simulate the water flow during the water impact of a rigid horizontal circular and an elastic cylindrical shell. Exact free surface conditions were satisfactory.

Ramos et al. (2000) conducted an experimental program assessing the slam induced loads on a segmented ship model that with several interconnected long wedges while the previous studies dealt with individual 2D wedges, which was analyzed with the method used by Ramos and Guedes Soares (1998).

Most investigations of water entry problems, including the researches mentioned above have been focused on the two-dimensional impact, while fewer study have been conducted on the three dimensional cases which is more consistent with the real impact in engineering. In this field, early studies have been published by some researchers. Shiffman and Spencer (1951) investigated the vertical slamming on spheres and cones based on the analytical solution. They are among the first to notice that the liquid may separate from the sphere, leading to cavity formation, however, the stage of the impact under consideration in this study is before separation which means the penetration depth is less than half of radius. Shiffman and Spencer (1951) also give an explicit relationship of impact coefficient with $f(\beta)=1.6$ for a cone with deadrise angle 30°. E1 Malki Alaoui et al. (2012) recently found the experimentally determined equivalent as $f(\beta)=1.58$ and the non-dimensional slamming coefficient $f(\beta)$ depends only on the deadrise angle β. By means of high-speed shock machine, they studied the slamming coefficient on axisymmetric bodies, and found that Cs for hemisphere, unlike the cones, depends on the depth of immersions.

Based on the Wagner's theory, Chuang (1967) developed an analytical formulation for the pressure distribution on a cone with small deadrise angle, and Faltinsen and Zhao (1997) proposed a theoretical method for water entry of hemispheres and cones with small deadrise angles. Battistin and Iafrati (2003) studied the impact loads and pressure distribution on axisymmetric bodies by numerical solution. In the field of experimental investigation, Chuang and Milne (1971) performed drop tests on the conical bodies, and recently Peseux et al. (2005) carried out the drop tests for cones with small deadrise angles which include 6°, 10° and 14°.

Motivated by the work of Stenius et al. (2006), who conducted the modeling of hydro elasticity in water impacts of ship bottom-panels by using LS-DYNA, Luo et al. (2011) and Wang et al. (2012) investigated the symmetric water impact of two-dimensional rigid wedge sections and ship sections, the predictions from which had very good agreement with comparable measured values and other numerical results by applying the explicit finite element method, and then the effects of the deadrise angle on the slamming load were presented in Wang and Guedes Soares (2012) and Wang et al. (Submitted for publication). They extended the research to the asymmetric water impact of a bow-flared section with various roll angles in Wang and Guedes Soares (2013). In the present work, the explicit finite element method is extended to study the hydrodynamic problem of three-dimensional bodies, including hemisphere and cones with different deadrise angles. The predictions are compared with the experimental results from the drop tests of De Backer et al. (2009) and theoretical calculations based on Wagner (1932)'s method, in terms of impact velocity, acceleration, penetration depth in the water and the pressure histories on the pressure sensors. The comparisons between them are satisfactory in the initial stage of the water entry. Then, the verified method is applied to estimate the impact coefficients on a falling hemisphere and a cone with a deadrise angle 30°, which show good consistency with some analytical and theoretical predictions.

2. Mathematical formulations

In this section, the equations that govern the fluid motion and the interaction between the fluid and structures in this explicit finite element method are recalled.

2.1. ALE description of Navier–Stokes equations

The governing equation for incompressible and unsteady Navier–Stokes fluid is described as:

$$\frac{\partial u}{\partial t}+u\nabla u-2u^F\nabla\varepsilon(u)+\nabla p=b \tag{2.1}$$

$$\nabla u=0 \tag{2.2}$$

where u is the flow velocity, p is the pressure of fluid, b means body force acting on the fluid and $\varepsilon(u)$ represents the deviatoric stress tensor.

The boundary condition and initial condition are

$$\sigma=-pI+2v^F\varepsilon(u) \tag{2.3}$$

$$\varepsilon(u)=\frac{1}{2}(\nabla u+(\nabla u)^T) \tag{2.4}$$

In ALE formulation, a reference coordinate which is not the Lagrangian coordinate and Eulerian coordinate is induced. The differential quotient for material with respect to the reference coordinate is described as following equation.

$$\frac{\partial f(X_i,t)}{\partial t}=\frac{\partial f(x_i,t)}{\partial t}+w_i\frac{\partial f(x_i,t)}{\partial x_i} \tag{2.5}$$

where, X_i is the Lagrangian coordinate, x_i is the Eulerian coordinate, and w_i is the relative velocity.

Therefore, the ALE formulation can be derived from the relation between the time derivative of material and that of reference geometry configuration.

Assume that v represents the velocity of the material, and u means the velocity of the mesh. In order to simplify the above equation, relative velocity w is induced, which is given by $w=v-u$. Therefore, ALE formulation can be obtained from following conservation equations:

(1) The mass conservation equation:

$$\frac{\partial\rho}{\partial t}=-\rho\frac{\partial v_i}{\partial x_i}-w_i\frac{\partial\rho}{\partial x_i} \tag{2.6}$$

(2) The momentum conservation equation
The governing equation of fluid is Navier-Stokes equation which is described by the ALE method:

$$\rho\frac{\partial v_i}{\partial t}=\sigma_{ij,j}+\rho b_i-\rho w_i\frac{\partial v_i}{\partial x_j} \tag{2.7}$$

The stress tensor is expressed by:

$$\sigma_{ij}=-p\delta_{ij}+\mu(v_{i,j}+v_{j,i}) \tag{2.8}$$

The initial and boundary conditions are:

$$v_i = U_i^0 \quad \text{on } \Gamma_1 \text{ domain} \tag{2.9}$$

$$\sigma_{ij} n_j = 0 \quad \text{on } \Gamma_2 \text{ domain} \tag{2.10}$$

while

$$\Gamma_1 \cup \Gamma_2 = \Gamma \Gamma_1 \cap \Gamma_2 = 0 \tag{2.11}$$

where, Γ represents the whole boundary of computed field, while Γ_1 and Γ_2 means the parts of Γ. n_i represents the unit vector of boundary in outward normal direction, δ_{ij} is Kronecker δ function. Assume that the velocity field at time $t=0$ in the whole computed domain is known as:

$$v_i(x_i, 0) = 0 \tag{2.12}$$

(3) The energy conservation equation

$$\rho \frac{\partial E}{\partial t} = \sigma_{ij} v_{i,j} + \rho b_i v_i - \rho w_j \frac{\partial E}{\partial x_j} \tag{2.13}$$

The Euler equation is derived based on the assumptions that the velocity of reference configuration is zero, and the relative velocity between the material and the reference configuration is the velocity of the material. The terms of velocity in the Equation (2.7) and the equation (2.9) are known as convective terms which are used to calculate the transportation volume that the material flows through the mesh. The additional items are the reason that the numerical solution of the ALE equation is much more difficult than that of a Lagrange equation in which the relative velocity is zero.

There are two approaches to solve the ALE equation, which are similar to the methods applied to Euler's viewpoint in hydrodynamics. The first method is solving fully coupled equations using computational fluid mechanics, which can only govern singular material in singular element. The second one was called detached operator method, of which the calculation in each time step is separated into two parts. First, the Lagrange approach is executed, when the mesh moves with material. During this process, the equilibrium equations are:

$$\rho \frac{\partial v_i}{\partial t} = \sigma_{ij,j} + \rho b_i \tag{2.14}$$

$$\rho \frac{\partial E}{\partial t} = \sigma_{ij} v_{i,j} + \rho b_i v_i \tag{2.15}$$

In the Lagrange process, there is no material flowing through element boundary, so the calculation satisfies the mass conservation. Then the transportation volume, internal energy and kinetic energy of materials that flow through the boundaries of element are calculated in the second stage. It can be considered as remapping the meshes back to their initial or arbitrary positions.

As to each node, the velocity and displacement are updated according to following equation:

$$u^{n+1/2} = u^{n-1/2} + \Delta t M^{-1} (F_{ext}^n + F_{int}^n) \tag{2.16}$$

$$x^{n+1} = x^{n-1} + \Delta t u^{n+1/2} \tag{2.17}$$

where, F_{int}^n is vector of internal force, and F_{ext}^n is vector of external force. They are in relation with body force and boundary conditions. M is diagonal matrix of mass.

2.2. Fluid-structure coupling algorithm

In an explicit time integration problem, after computation of fluid and structure nodal forces, the coupling forces of the nodes on the fluid structure interface are computed in the time step. For each structure node, a depth penetration $\vec{d}$ is incrementally updated at each time step, using the relative velocity $(\vec{v_s} - \vec{v_f})$ at the structure node, which is considered as a slave node, and the master node within the Eulerian element. The location of the master node is computed using the isoparametric coordinates of the fluid element. At time $t = t^n$, the depth penetration $\vec{d}^n$ is updated by:

$$\vec{d}^{n+1} = \vec{d}^n + (\vec{v_s}^{n+1/2} - \vec{v_f}^{n+1/2}) \Delta t \tag{2.18}$$

where Δt is the increment of time, $\vec{v_s}$ is the velocity of the slave node, $\vec{v_f}$ is the fluid velocity at the master node location, interpolated from the nodes of the fluid element at the current time, and the vector $\vec{d}^n$ means the penetration depth of the structure inside the fluid during the time step. The coupling force acts only if penetration occurs.

Penalty coupling behaves like a spring system and penalty forces are calculated proportionally to the penetration depth and spring stiffness. The head of the spring is attached to the structure or slave node and the tail of the spring is attached to the master node within a fluid element that is intercepted by the structure. Similarly to penalty contact algorithm, the coupling force is described by:

$$F = kd \tag{2.19}$$

where k represents the spring stiffness, and d means the penetration. The coupling force F is applied to both master node and slave node in opposite direction at the coupling interface. The main difficulty in the coupling problem is the evaluation of the stiffness k.

In this paper, the stiffness of the spring is based on the explicit penalty contact algorithm in LS-DYNA, and the numerical stiffness by unit area is given in term of the bulk modulus K of the fluid element in the coupling containing the slave structure node, the volume V of the fluid element that contains the master fluid node, and the average area A of the structure elements connected to the structure node.

$$k = p_f \frac{KA}{V} \tag{2.20}$$

However, to avoid numerical instabilities, a penalty factor p_f is introduced for scaling the estimated stiffness of the interacting (coupling) system. For impact problems, it is always necessary to examine the influence of this parameter on the solution (Aquelet et al. (2006)). For the problem of two-dimensional wedge, Luo et al. (2011) conducted a parametric study, including the penalty factor, time step factor, mesh size and the number of the contact points, and validated this method by comparing the predictions with the experimental results from Zhao et al., 1996. The results show that mesh size is of great importance for the simulations, while other aspects affect little.

3. Numerical modeling

3.1. Description of the 3D structures

In this work, different kinds of three-dimensional structures, including a hemisphere and cones with different deadrise angles are studied. To validate the method used in present work, the predictions from a hemisphere, a cone20° and a cone45° entering calm water with drop velocity, are compared with the measured values from De Backer et al. (2009). The main parameters of the tested bodies which are applied in the numerically modeling, are listed in Table 1. As seen, the diameters of the bodies are 30 cm which is considered sufficient to reduce surface tension effects.

Since the structures are made from polyurethane and the material thicknesses are large, the deformations of them during the water impact are considered limit. It must be noted that the measured initial velocities listed in Table 1 are lower than the theoretical calculations based on the drop heights due to the friction in the guiding system of the test.

The pressure time history, the position and deceleration of the body were recorded in this test work. Pressure sensors were used to obtain the pressure time history on the body. The sensors were located at a horizontal distance of 0.04–0.09 m on the bodies from the symmetric axis respectively, as plotted in Fig. 1, in which P1 and P2 represent the pressure sensors and β is the deadrise angle of the cones.

Besides, non-dimensional impact coefficients on hemisphere and cones with different deadrise angles are computed based on the assumption of constant impact velocity. They are compared with available measured and numerical values as well.

3.2. Description of the modeling

The explicit finite element analysis is based on a multi-material Eulerian formulation and a penalty coupling method. The fluid is solved by using a Eulerian formulation, while the wedge is discredited by a Lagrangian approach. The fluids (water and air) are defined as the multi-material group, which means that the effects of the water and the air are all considered. The penalty coupling algorithm is applied to activate the interaction between the fluids and the structure. It behaves like a spring system, thus generating high oscillations to the coupling force. The penalty forces are calculated proportionally to the penetration depth and spring stiffness. Though some noise will be generated to the pressure values on the Lagrangean elements, the total force on the structure will not be sensitive to the coupling factor, since it is an average value. The commercial code LS-DYNA is used as a tool to solve the differential equations that govern the phenomenon with following hypotheses:

- The gravity effects are neglected.
- The surface tension effects will not be modeled.
- The structures have no deformation and rotate motion.

Table 1
Characteristics for the measured bodies.

Item	Radius (m)	Total mass (kg)	Material thickness (m)	Initial Velocity (m/s)
Hemisphere	0.15	11.5	0.05	4.0
Cone 20°	0.15	9.8	0.03	3.85
Cone 45°	0.15	10.2	0.03	4.05

Based on these assumptions, the numerically modeling is as follows:

- The coordinate system of the problem
  As illustrated in Fig. 2, a Cartesian coordinate system (x, y, z) is introduced, and the (x, y)-plane is placed in the undisturbed water surface, while the z-axis is located in the axis of the body. The body enters the calm water with a vertical velocity which is denoted as dz/dt, and $t=0$ means the time instance when the body touches the water. The boundaries of the water are denoted as S_L, S_R and S_B .

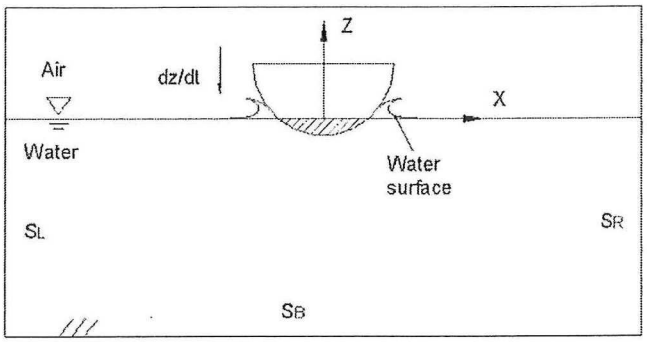

Fig. 2. Coordinate system of the problem.

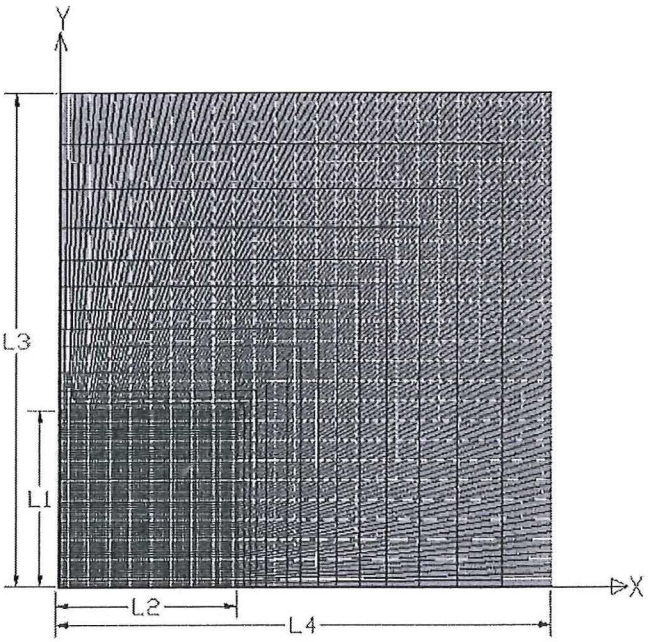

Fig. 3. Mesh style of the fluids in the x–y plane.

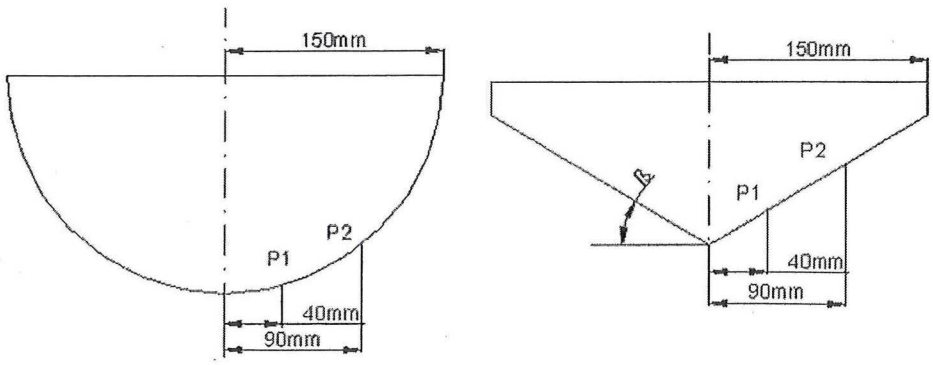

Fig. 1. Locations of the pressure sensors (mm).

- The material and element types
  The fluid, water and air, are modeled with Solid164 element which is an 8-nodes brick element, and they are defined as void materials which allows equations of state to be considered without computing deviatoric stresses. The Gruneisen equation of state is used to the water domain and the linear polynomial equation of state is applied for the air domain. The wedge is modeled with Shell163 element which is a 4-nodes element and can only be used in explicit dynamic analysis, and rigid body material.
- Boundary conditions
  Only a quarter of the model is established with symmetric boundaries on (y–z) and (x–z) planes. The boundaries of the fluids are defined as non-reflecting, except that, other fluids nodes are free. For the body, only vertical movement downwards is released.
- Numerical model
  As known, the ALE calculation is time-consuming, so different mesh types are applied on different regions to reduce memory and CPU requirement. Luo et al. (2011) found that the mesh size in the region near the contact area between the structure and the fluids are of great importance to the simulation. As to the region that is far from the impact, the mapped area mesh which contains only quadrilateral elements is employed, and the mesh size in this domain is moderately expanding towards the boundaries. Fig. 3 and Fig. 4 show the mesh style of the fluids in x–y and y–z planes. Furthermore, the structure is meshed with quadrilateral elements as plotted in Fig. 5. Considering the computational efforts, the fluids domain is limited to 0.5 m × 0.5 m × 0.6 m, which means the dimension in x–y plane is $L4 \times L3$ (0.5 m × 0.5 m), and the dimensions of air domain and water domain in z-direction are $L7+L8$ (0.2 m+0.4 m). The dimension of impact domain is denoted as $L1 \times L2 \times (L5+L6)$ which is 0.18 m × 0.18 m × (0.05 m × 0.08 m). It is found that the size of the impact domain′ is of great importance to the numerical results. The selection of the size of the model in present work is based on lots of calculations and the experience using the code. The discussion on the models with different size is not presented here, because the convergence study focuses on the mesh density and the contact stiffness.

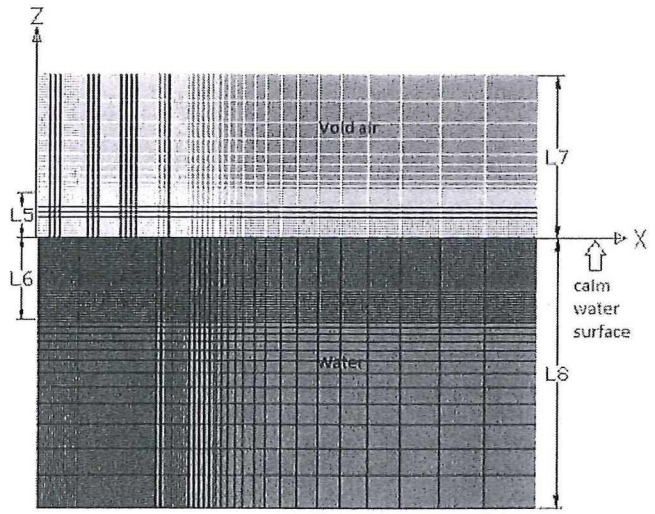

Fig. 4. Mesh style of the fluids in the y–z plane.

For modeling accurately of the water impact problem, a careful selection of mesh density and contact stiffness is required. As mentioned in Section 2.2, the contact stiffness is related to the penalty factor and the volume V of the fluid element that contains the master fluid node, so it is affected by the mesh density of the fluids. In the following section, a convergence study is conducted to obtain a proper numerical model.

4. Convergence study

4.1. Mesh density

Three mesh sizes,10 mm, 5 mm and 2.5 mm are selected for the fluids of the impact domain ($L3 \times L4 \times (L5+L6)$). The mesh sizes are denoted by 0.067R, 0.033R and 0.0167R, where R means the radius of the hemisphere or the cones. Unless otherwise specified, the mesh size of the structure is as same as that of the fluids, and the value of p_f is set as 0.1. In present work, the numerical contact stiffness k is computed by equation (2.20). For the three models, the value is 22.5 Gpa/m, 45 Gpa/m and 90 Gpa/m, respectively.

Fig. 6 presents the predicted non-dimensional impact coefficients of a rigid hemisphere of radius R entering vertically into initially calm water with a constant velocity V, together with the available experimental and numerical results. The non-dimensional impact coefficient is defined as $C_S = 2F/\rho\pi R^2 V^2$, where F is the total impact force and $\rho = 100$ kg/m^3 is the density of the fluid, and the non-dimensional time is denoted as $d(t)/R$, where $d(t)$ is the instantaneous penetration of the sphere below the calm water. Here, the impact velocity is 4 m/s, and the radius

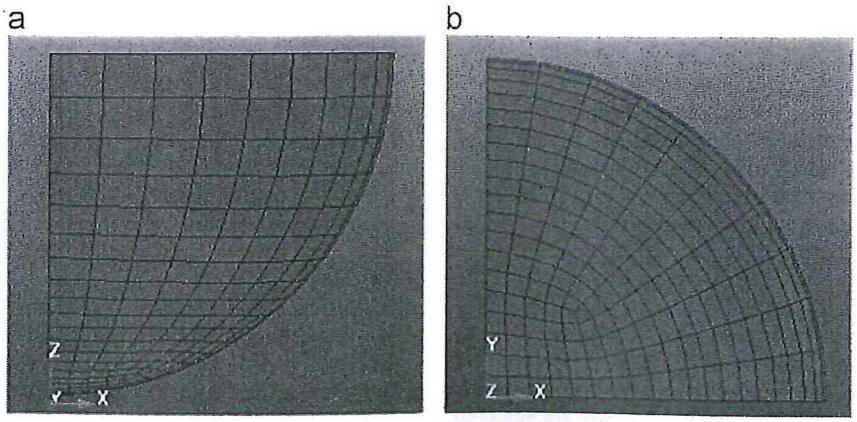

Fig. 5. Mesh style of the structure.

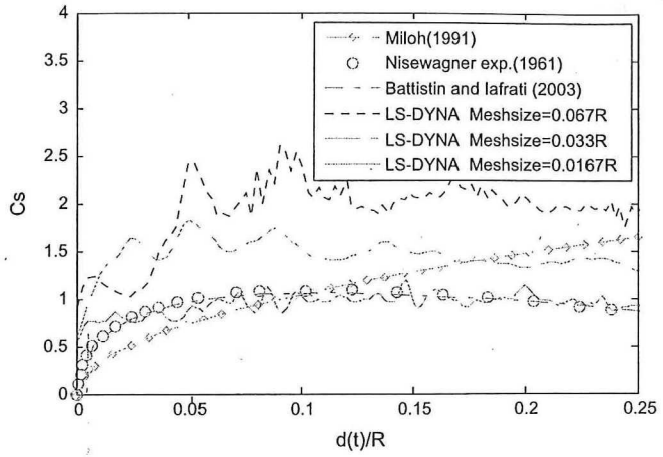

Fig. 6. The impact coefficient for a rigid hemisphere impacting with calm water.

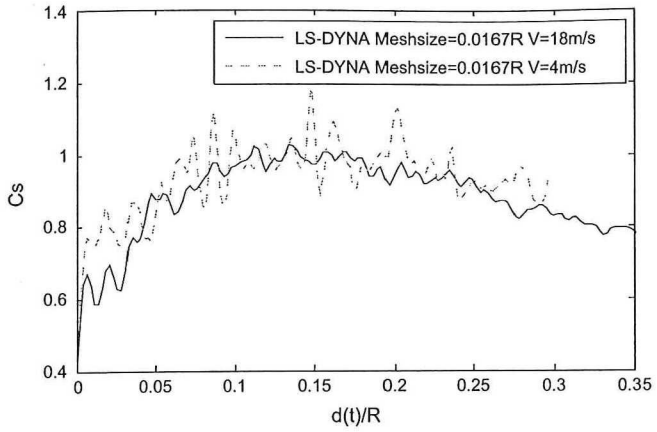

Fig. 7. The impact coefficient for rigid hemisphere entering calm water with different velocities.

Table 2
Three models with different mesh densities.

Parameters	Model 1	Model 2	Model 3
Mesh size	0.067R	0.033R	0.0167R
Number of elements(Fluids)	43200	134400	510300
Number of elements (Structures)	175	500	1600
CPU time[a]	1 h 22 min	9 h 49 min	45 h 53 min

[a] *Note*: It was run on one PC with 2.50 GHz processor and 3 Gigabytes of memory.

of the sphere is 0.15 m. Table 2 lists the main parameters for the three models with 0.015 s′ solution time.

As seen in Fig. 6, when the mesh size is 0.0167R, the predicted impact coefficient is in good agreement with the experimental measurements from Nisewanger (1996) and the numerical calculations from Battistin and Iafrati (2003), after the initial stage of the impact. At the initial stage, the impact coefficient is higher than the experimental and numerical results. This is because, at this stage, the interaction between the fluid and the structure only involves few elements, from the bottom of the hemisphere and the surface of the water. The numerical impulses of pressure on the elements are inevitable at the initial impact, and the impact force is obtained from the integration of the pressures along the wetted surface of the structure. For the analytical calculations from Miloh (1991), the simplified method gives lower predictions at the initial stage and higher ones at the late stage.

When the mesh size is 0.033R and 0.067R, the predictions are not consistent with the experimental measurements. At the middle and late stage of the impact, as the mesh size becomes large, the impact coefficient is higher. It also shows that the numerical noises are apparent for a larger mesh size.

It is obvious that the model with 0.0167R mesh size is more appropriate to capture the time history of impact force on the hemisphere entering calm water, and the computational time is acceptable. To verify the stability of the numerical results, different impact velocities are applied to the hemisphere. The impact coefficients on the hemisphere with $V=4$ m/s and $V=18$ m/s are plotted in Fig. 7, which shows very good consistency. The discrepancy at the initial stage is still due to the mesh size.

To capture the pressure distribution on the hemisphere surface, virtual pressure sensors are located at the center of the shell elements on location $y=0$. The hemisphere is meshed with 4799 shell elements, from which 80 elements on x–z plane are selected. Fig. 8 shows the pressure distributions on the wetted hemisphere

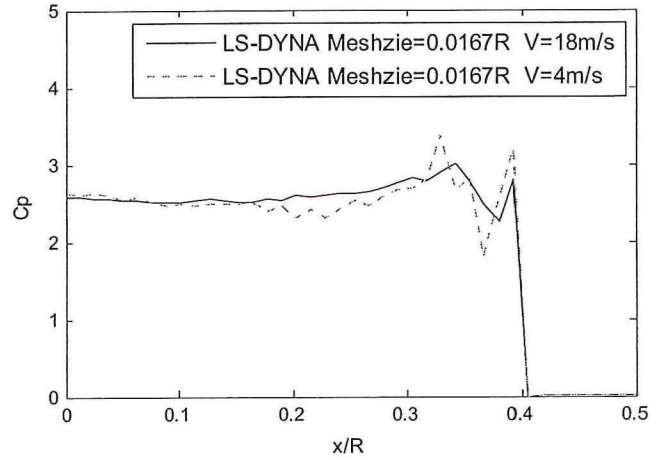

Fig. 8. The impact coefficient for a rigid hemisphere impacting with calm water at $d(t)/R=0.134$.

surface on x–z plane *at* $d(t)/R=0.134$. The non-dimensional pressure Cp is defined as $2p/\rho V^2$, where p is the pressure value obtained from the pressure sensor. x/R denotes the position on the hemisphere surface, where x is the coordinate of the element and R is the radius. $x/R=0$ means the lowest point, and $x/R=1$ is the highest point on the hemisphere. For different impact velocities, the pressure distributions have very good agreement. Some numerical noise is observed at the position near the intersection between the water surface and the structure for both cases. At this moment, the pressure is almost uniformly distributed along the surface.

The predictions of impact coefficient and pressure distribution from the model 0.0167R with different impact velocities show very good consistency. It is believed that this model is appropriate for the hemisphere.

Fig. 9 plots the predicted non-dimensional impact coefficients of a cone20° of radius R entering vertically into initially calm water with a constant velocity V. Here, the mesh size of the structure is 0.0167R for the three models, so the numerical contact stiffness is respectively, 1.406 Gpa/m, 11.25 Gpa/m and 90 Gpa/m. Similar to the predictions of the hemisphere, the impact coefficient is higher for a model with larger mesh size. When the mesh size is 0.0167R and 0.033R, the numerical calculations are close, especially for the values at the middle stage. At the late stage, a high impulse is observed in the curve of the model with 0.067R mesh size. This is

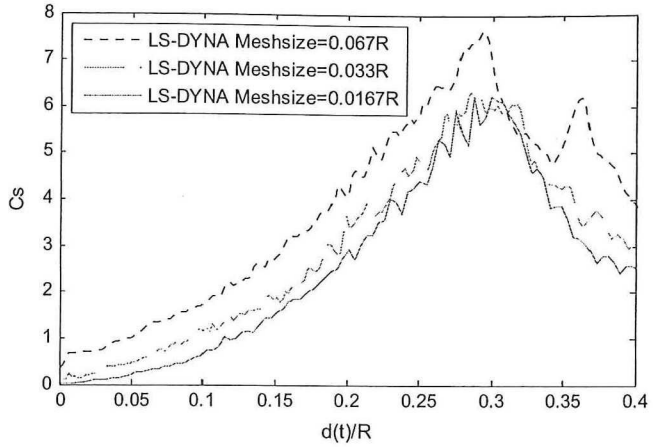

Fig. 9. The impact coefficient for a cone20° impacting with calm water.

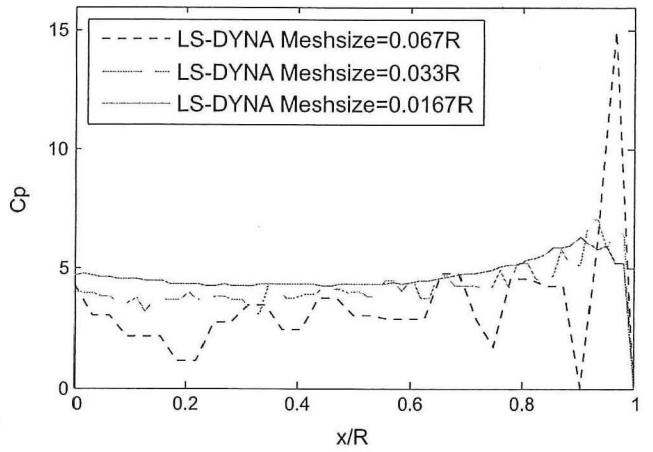

Fig. 10. Pressure distribution along the surface of cone20° at t_{max}.

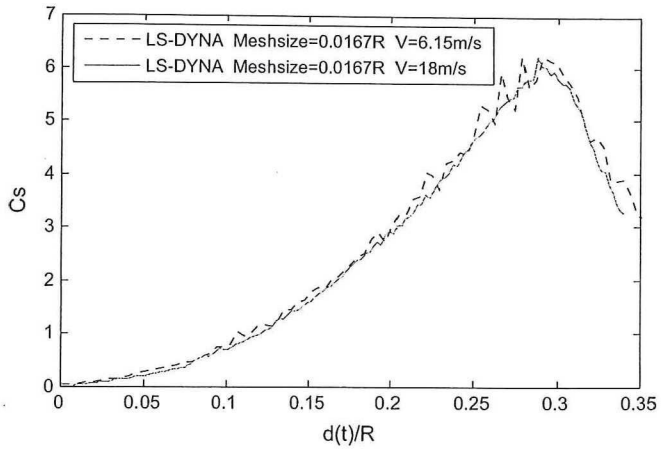

Fig. 11. The impact coefficient for a cone20° impacting with calm water at different velocity.

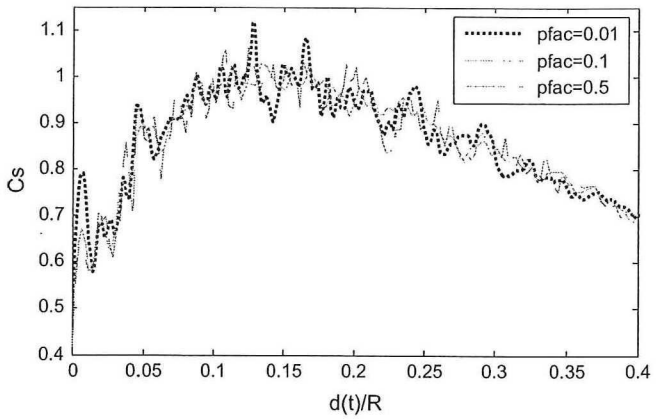

Fig. 12. The impact coefficient for a hemisphere impacting with calm water with different value of pfac.

because the mesh size of water surface nearby the structure surface becomes larger as the water surface evolves during the impact. For a cone20° with $R=0.15$ m, and $v=6.15$ m/s, the total immersion occurs at $t=0.0089$ s while $t=0$ s means the cone touches the calm water. As seen for the three models, the maximum impact force occurs at about $d(t)/R=0.29$, and the corresponding time instant $t=0.00707$ s which is in good agreement with Wagner's theory predicting $t_{max}=\pi R\tan\beta/4V=0.007$ s.

Fig. 10 shows the pressure distribution on the wetted surface of cone20° on x–z plane *at* t_{max} (the time instant when the peak value happens). The pressure value is obtained even at the highest point. This means the water jet is produced under the structure's surface and reaches the highest position. The present method's predictions show that the maximum impact force on a cone 20° occurs at the total immersion of the model.

As seen from the three curves, the maximum pressures are located near the root of the water jet. This is consistent with the result obtained from the 2D wedge 20° before flow separation. When the mesh size is 0.067R, the pressure distribution obtained from the sensors has much noise and the pressure values are much lower than the ones from the models with 0.033R and 0.0167R mesh size. When the mesh size is 0.033R or 0.0167R, the pressure distributions are in good agreement, however, the one from the model with 0.0167R mesh size is smoother.

The impact coefficients on the cone20° with different impact velocities are plotted in Fig. 11. The predictions have good agreement, while the curve from the model with $V=18$ m/s is smoother.

4.2. Contact stiffness

As mentioned before, a penalty factor p_f (pfac) is introduced for scaling the estimated stiffness of the coupling system. To obtain a proper value of it, the influence of this parameter on the solution is examined. Through the sensitivity study of mesh size, the model with 0.0167R mesh size is selected for water impacts of the hemisphere and cones, and for the model, the default value of pfac is 0.1. Here, two different values, 0.01 and 0.5 are applied in the simulations.

Fig. 12 plots the impact coefficients on the hemisphere with different pfac values. Here, the mesh size is 0.0167R, and the constant impact velocity is 18 m/s. Generally speaking, the three curves agree well, though some oscillations exist. Obvious distinctions are observed at the initial moment of the impact and at the moment that the peak value occurs. As seen in Fig. 6, the impact coefficient from the model with 0.0167R mesh size, the contact stiffness of which is 90 Gpa/m, agrees well with the experimental measurements, compared to the models with lower contact stiffness. It seems that higher contact stiffness is better for the impact model of the hemisphere. However, for the model with 0.5 pfac, the curve of impact coefficient does not become better, and even appears more numerical noises.

The 80 pressure sensors, which are located at the center of the shell elements on x–z plane, are numbered from 1 to 80, in which sensor 1 means the lowest one and sensor 80 denotes the highest one. The pressure values captured by three sensors are shown in Fig. 13. The results show that the maximum local pressure value is

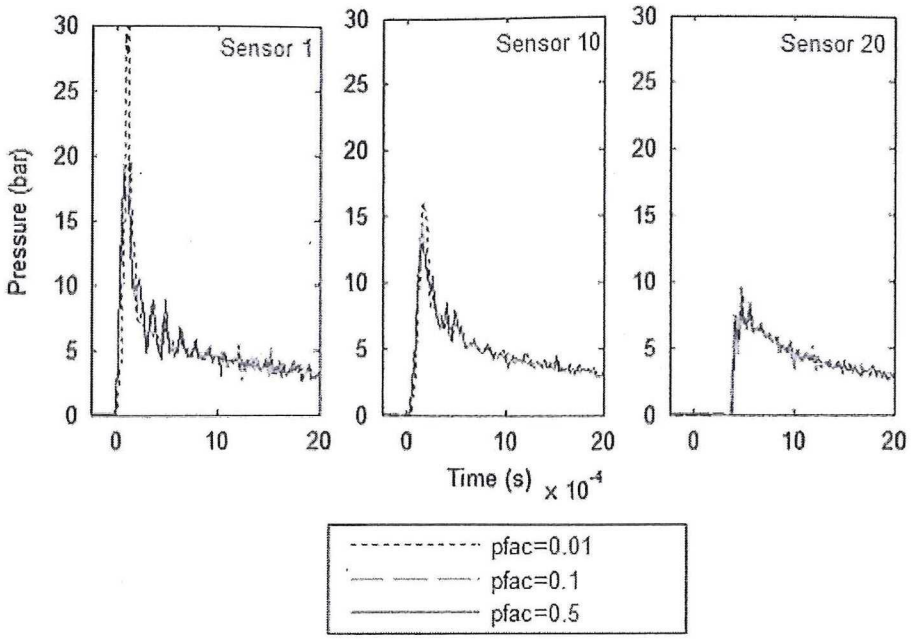

Fig. 13. Pressure histories on the bottom surface of the hemisphere.

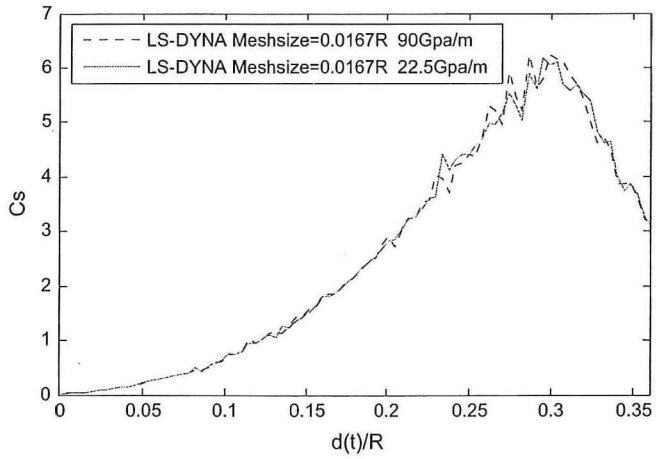

Fig. 14. The impact coefficient for a cone20° impacting with calm water with different contact stiffness.

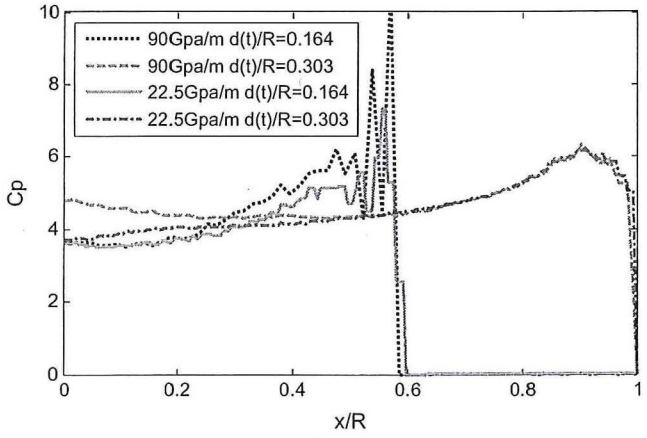

Fig. 15. Pressure distribution along the surface of cone20° at two time instants.

located at the lowest point of the hemisphere. As the distance from the point to the axis of the hemisphere becomes far, the local peak pressure decreases greatly.

It is found that the local peak pressure on the hemisphere is sensitive to the value of pfac. The higher the contact stiffness is, the smaller the peak value is. These differences become small when the position of the sensor is higher. From the pressure histories, it is also possible to find that the maximum pressure value occurs at the moment when the hemisphere touches the calm water, during the water impact.

The peak values are sensitive to the scale factor. This is consistent with the fact that the coupling force on the master and slave node is computed by multiplying contact stiffness and penetration, while the contact stiffness is scaled by the value of pfac. The total impact forces on the structure are not sensitive to the variation of the scale factor, since they are average values on the structure.

For the models of the cone20°, the one with 0.0167R mesh size is studied here, firstly by altering the mesh size of the Lagrangian elements, and secondly by applying different values of pfac, to investigate the influences of the contact stiffness. Based on Eq. (2.20), the numerical contact stiffness is 22.5 Gpa/m, when the mesh size of the cone is 0.00835R. The predicted impact coefficient and pressure distributions on the wetted surface of cone 20° are compared with the calculations from the model with k=90 Gpa/m, as shown in Figs. 14 and 15.

The impact coefficients have very limited differences, while some noise is observed in both curves. In Fig. 15, the pressure distributions at two time instants $d(t)/R$=0.164 and $d(t)/R$=0.303 are presented. At the former time instant, the only half of the structure immerses into the water surface, while at the later time instant, the structure immerse into the water completely, considering the water surface elevation. It can be found that, before flow separation, the maximum pressure is located at the lowest point of the cone. With different contact stiffness, the general trends of the pressure distribution do not change too much. Only some differences are observed near the spray root of the water surface or at the lowest lower part on the cone surface. Unlike the simulations of the hemisphere, the pressure values are larger when the contact stiffness is higher for the cone20°.

Figs. 16 and 17 show the impact coefficients and pressure distributions on the cone20° with different value of pfac. The influences of the scale factor on the results are small, though slight

differences are found around the middle stage of the impact in the curves.

4.3. Time step

An ALE formulation consists of a Lagrangian time step followed by an advection step, which updates the velocity and displacement on each node at one time step. A stable time step is of great significant to the numerical results. The time step should not be larger than the critical one, otherwise negative volume errors will appear. But if the time step is set to one value that is too small, then the computational time will increase correspondently. The critical time step size is the minimum time value that the sound travels through any elements in the model. The critical time step size can be approximated firstly before the simulation, in order to set one scale factor to obtain one appropriate time step. In LS-DYNA Theory manual, time step calculations for different types of elements are explained through mathematical formulations.

Obviously, the critical time step is related to the minimum size of the element, and the scale factor is between 0 and 1. For one numerical model, a proper time step value can be achieved by adjusting the scale factor. In present work, the time step for the models with 0.067R mesh size is 4.69E-07s, and the value is 2.28E-07s for the models with 0.033R mesh size, 1.14E-07s for the models with 0.0167R mesh size. It is found that the value is proportional to the mesh size. When the impact velocity is 18 m/s, the numerical solution time is decreased greatly, so a very small scale factor 0.05 is applied to make the solution stable, which follows a very small time step 5.71E-08s.

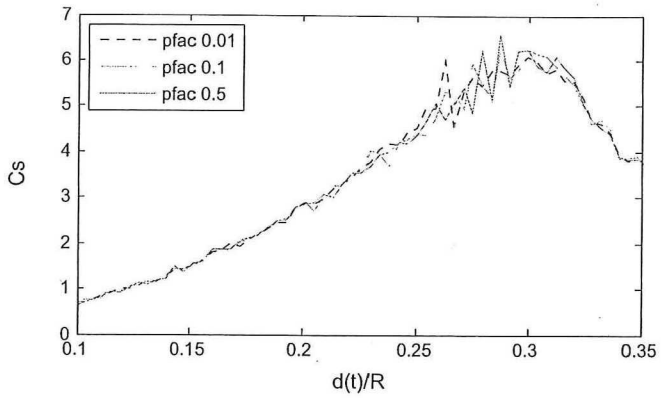

Fig. 16. The impact coefficient for a cone20 impacting with calm water with pf.

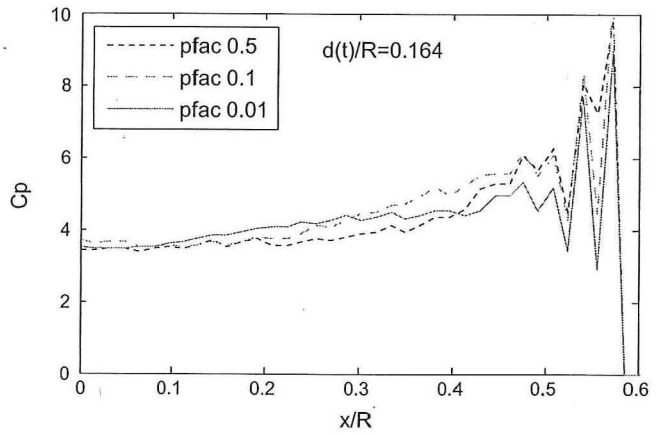

Fig. 17. Pressure distributions on the surface of cone20 at $d(t)/R=0.164$ for different

5. Validation and results

According to the drop tests of the three dimensional bodies De Backer et al. (2009), the acceleration, impact velocity, penetration depth and pressure distributions during the water impact are predicted and compared with the measured values, as well as the calculations from asymptotic theory. In order to reduce the influence of the assumptions mentioned above, only the initial stage of the impact is investigated. Furthermore, the impact coefficients on the hemisphere and cones are computed and compared to some published results, with the assumption of constant impact velocity. To examine the influences of this assumption, the predictions from the model with drop velocity and constant velocity are compared firstly.

5.1. Influence of impact velocity

Fig. 18 compares the impact coefficients on the hemisphere with different types of impact velocity. Two velocities $v=4$ m/s and $v=18$ m/s are selected. As seen, at the initial stage, the impact coefficients from two models agree well, while the differences between them become larger as the penetration depth raises. For a higher impact velocity, the influences are more apparent. Obviously, the impact force on a hemisphere entering with a constant velocity is higher, since that the impact velocity of the drop case decays due to the resultant force on the structure.

Fig. 19 compares the impact coefficients on the cone20 with different types of impact velocity. As seen, at the initial stage, the

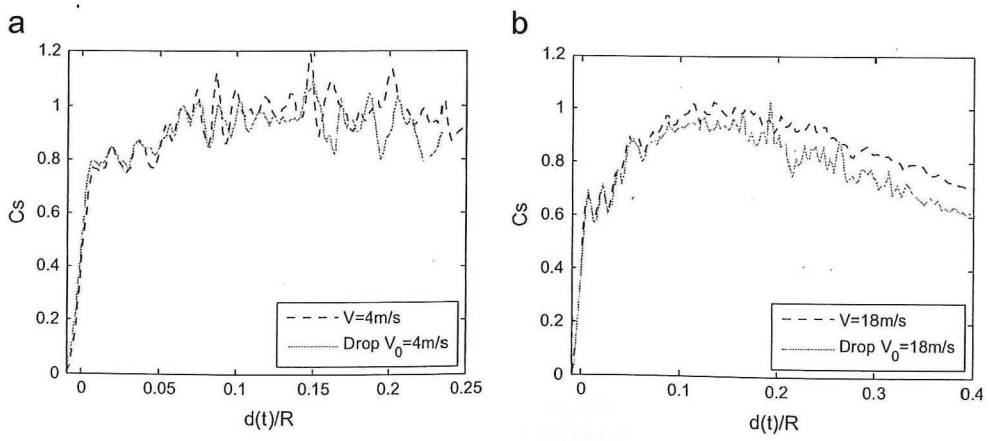

Fig. 18. Comparison of impact coefficients on the hemisphere entering water with constant and drop velocity.

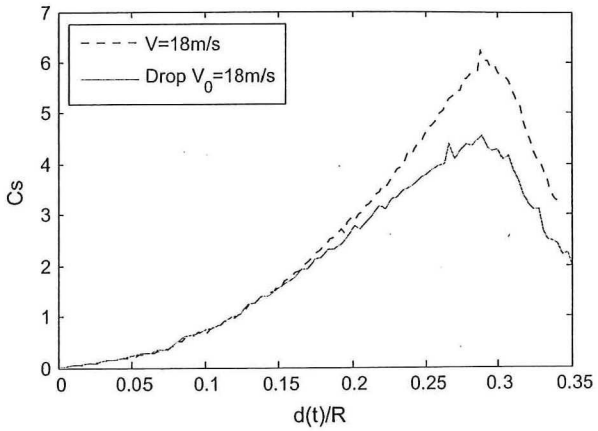

Fig. 19. Comparison of impact coefficients on the cone20° entering water with constant and drop velocity. $V=18$ m/s.

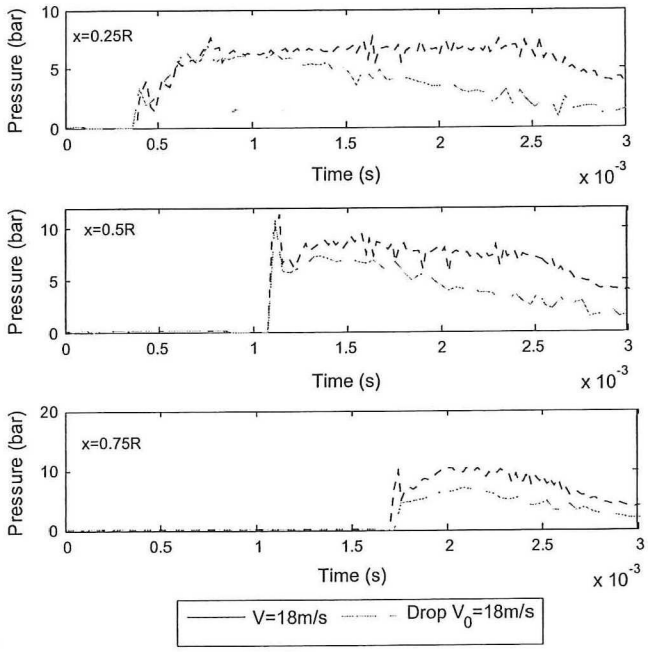

Fig. 20. Comparison of pressure histories on the cone20° entering water with constant and drop velocity. $V=18$ m/s.

impact coefficients from two models agree well, while the differences between them become larger as the penetration depth raises. The peak value from the model with constant velocity is much larger, although the non-dimensional penetration depths of the cone under water are very close when the peak values occur. The differences between the impact forces are due to the pressures on the wetted surface of the structure. Fig. 20 shows the pressures of three positions, which are denoted by $x=0.25R$, $x=0.5R$ and $x=0.75R$, on the cone in x–z plane. For the model with a dropt velocity, the pressure decays more quickly after the peak value occurs. Thus, the differences become larger as the impact processes.

5.2. Drop 3D structures

5.2.1. Hemisphere

Fig. 21 shows the predicted, measured and theoretical acceleration of the hemisphere during 0.012s after the bottom of the body touches water. The theoretical calculations are based on the

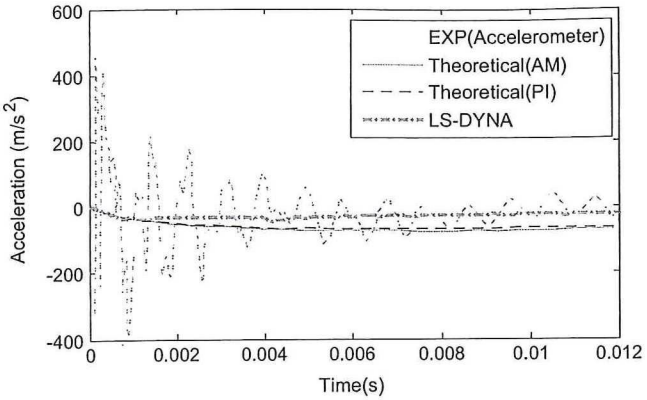

Fig. 21. Predicted and measured acceleration on the hemisphere.

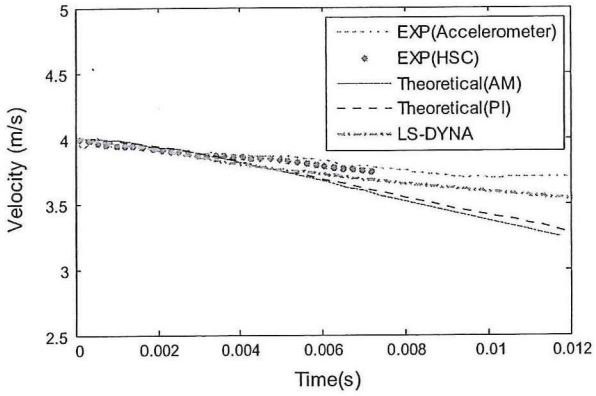

Fig. 22. Predicted and measured impact velocity on the hemisphere.

pressure integration method and added mass method. Although the experimental data has lots of high frequency noises, the prediction of LS-DYNA agree well with it, while the theoretical calculations overestimate the acceleration of the structure.

As plotted in Fig. 22, the impact velocity obtained by LS-DYNA is lower than that measured in the test, and the difference between them becomes larger as time goes by, mainly due to the friction created from the freely movement of the structure along the guiding system in the test. As expected, the hemisphere drops more quickly from the point of view of theoretical solutions. Correspondingly, the penetration depths below the calm water during this time span of the hemisphere are compared in Fig. 23, which also shows that the deviation between the measured value and the predicted ones from present work and theoretical solutions are observed more obviously as time progresses.

Fig. 24 plots the pressure histories of the two points at $r=4$ cm and $r=9$ cm on the hemisphere as illustrated in Fig. 1. As mentioned in Wang et al. (2012), the asymptotic theory overestimates the pressure of ship-like sections, in particular for a small deadrise angle, the similar behavior is observed here for both of the pressure points. For the pressure point at $r=9$ cm, the predictions from LS-DYNA are in good agreement with the measured ones, including the rising time of the peak value and as well the maximum value of the pressure, though some numerical noises exist. As to the pressure point at $r=4$ cm, the predicted peak value is smaller than the measured one. This is mainly due to the three-dimensionality of the simulation, for which the pressure captured by the virtual sensor is more easily disturbed by frequency noises, and probably the pressure is affected by the position of the sensor.

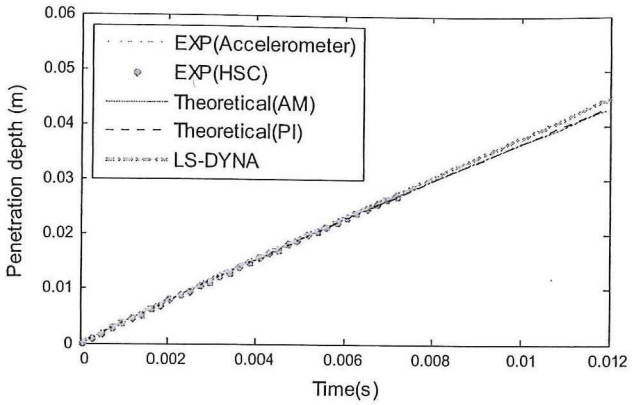

Fig. 23. Predicted and measured penetration on the hemisphere.

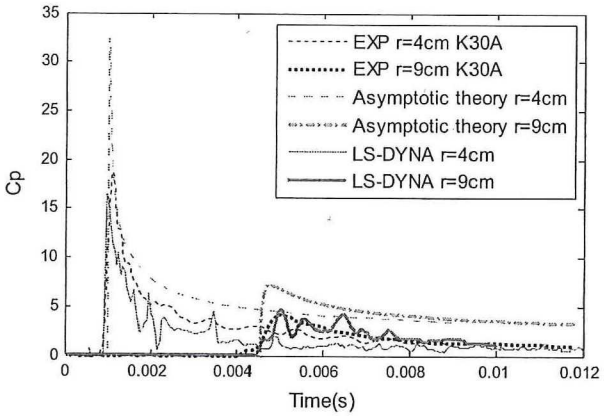

Fig. 24. Predicted and measured pressure distribution at $r=4$ cm on the hemisphere.

5.2.2. Cone 20°

Figs. 25–27 show the predicted and measured acceleration, impact velocity and penetration depth for the rigid cone with a deadrise angle of 20° during the impact. The comparisons between the calculations in this work with the measured and theoretical values are similar to that of the hemisphere.

Fig. 28 plots the pressure histories of the two points at $r=4$ cm and $r=9$ cm on the cone 20°. The simulated rising time of the pressure points at $r=4$ cm is a little bit earlier than those from the tests. Probably it is due to water jet of the free surface in the modeling, which affects the pressure value earlier. For the peak values, the one at $r=4$ cm is smaller than that from the experimental and theoretical solution, and this difference was also observed in the study of 2D wedge with a deadrise angle 20° by Wang and Guedes Soares (Submitted for Publication). Similar to the experiments, the predicted peak pressure at $r=9$ cm is larger than the one at $r=4$ cm.

5.2.3. Cone 45°

Figs. 29–31 show the predicted and measured acceleration, impact velocity and penetration depth for the rigid cone with a deadrise angle of 45° during the impact. Quite good agreements between the predictions and measured values are found in the initial stage, while the discrepancies increase as time goes by.

Fig. 32 plots the pressure histories of the two points at $r=4$ cm and $r=9$ cm on the cone 45°. Obviously, the predicted pressure peak at $r=4$ cm is much lower than the experimental results. It can be noticed that the rising time of the simulated pressure at $r=9$ cm is earlier than the measured and asymptotic ones.

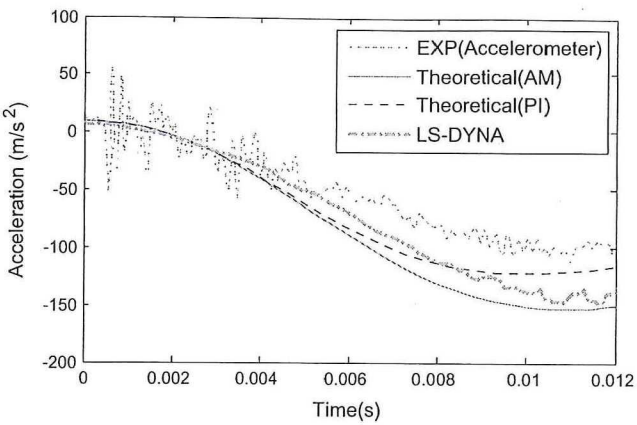

Fig. 25. Predicted and measured acceleration on the cone20 .

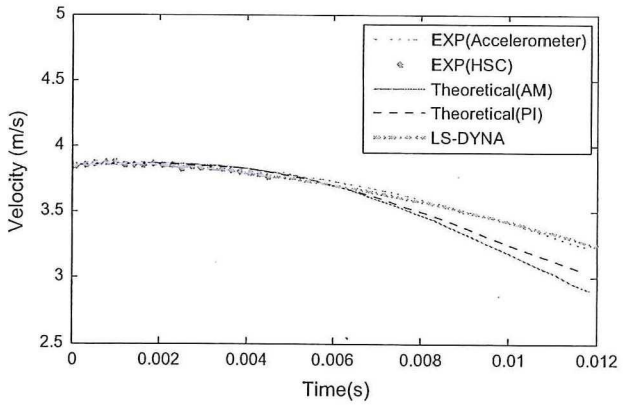

Fig. 26. Predicted and measured impact velocity on the cone20 .

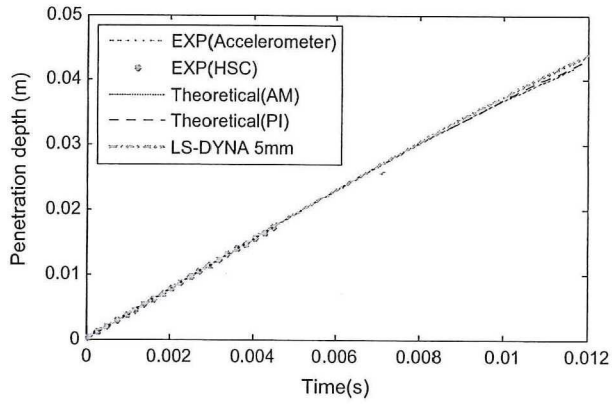

Fig. 27. Predicted and measured penetration on the cone20 .

Probably, it is due to the water surface elevation during the impact. High impulses are observed for these two pressures.

5.3. Impact coefficient

The non-dimensional impact coefficient on a hemisphere is plotted in Figure and compared with experimental measurements and numerical calculations. It must be noted that the impact velocity of the hemisphere is constant here.

As seen in this figure, the prediction in present work has good consistency with other calculations at the late stage. At the early stage, the present method underestimates the impact coefficient. This is consistent with the prediction of the pressure values at $r=4$ cm which are plotted in Fig. 24. It is due to the mesh size of

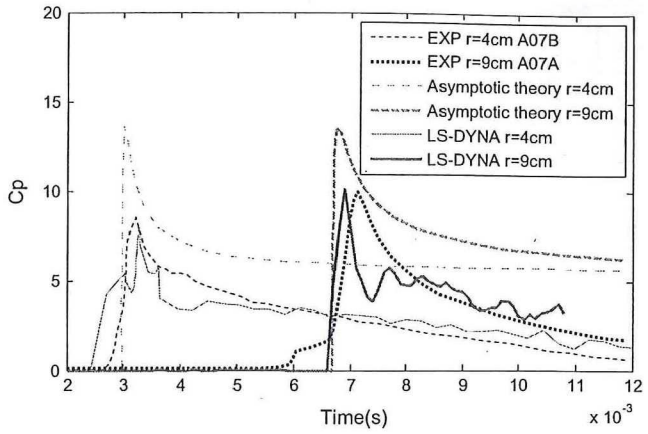

Fig. 28. Predicted and measured pressure distribution at $r=4$ cm on the cone20°.

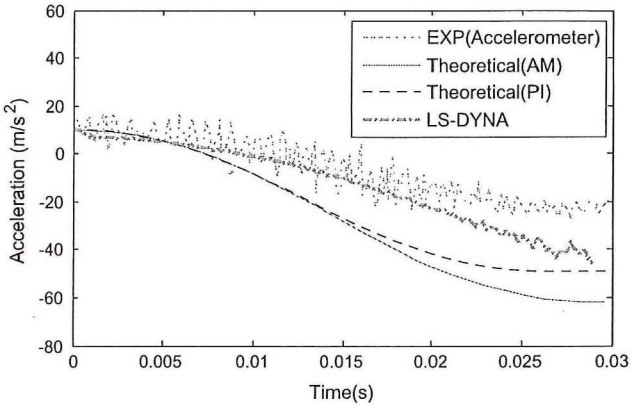

Fig. 29. Predicted and measured acceleration on the cone45°.

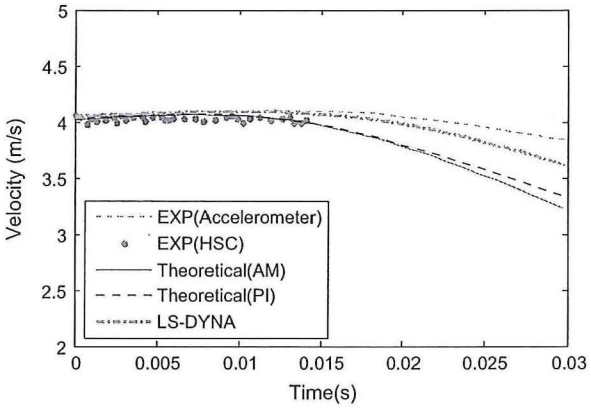

Fig. 30. Predicted and measured impact velocity on the cone45°.

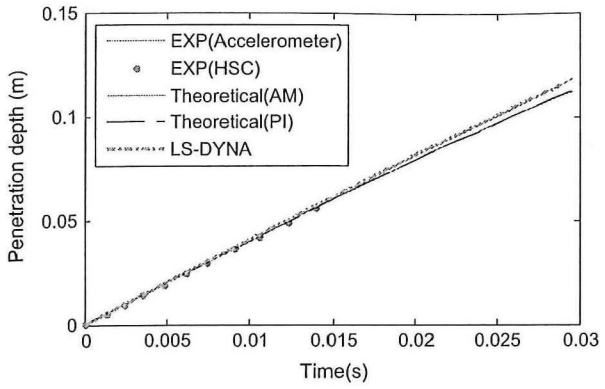

Fig. 31. Predicted and measured penetration on the cone45°.

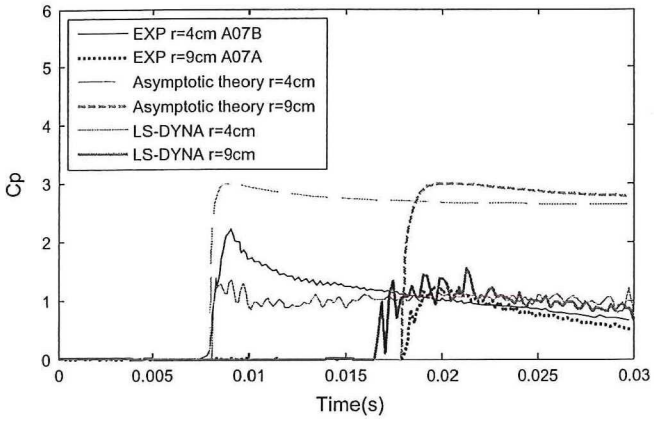

Fig. 32. Predicted and measured pressure distribution on the cone45°.

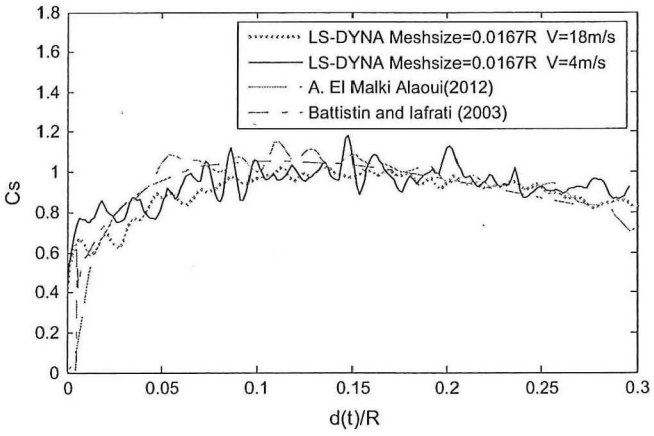

Fig. 33. Non-dimensional impact coefficient on a falling hemisphere.

the hemisphere and that of fluids in impact domain, and the contact stiffness between the coupling nodes.

Fig. 34 compares the predicted impact coefficient on the cone 30° with the calculations obtained from E1 Malki Alaoui et al. (2012)'s experiment. Good agreement is achieved between them. The pressure distribution on the wetted surface of the cone30° is compared with the calculations of Battistin and Iafrati (2003) in Fig. 35, in terms of non-dimensional pressure coefficient $Cp=2F/\rho V^2$ and relative position on the bottom surface $z/d(t)$, where z means the vertical coordinate of the position, and $d(t)$ is the instantaneous penetration of the cone below the calm water. $z/d(t)=-1$ denotes the lowest point of the cone, and $z/d(t)=0$ means the intersection between the cone and water. As plotted, the predicted water surface elevation is in good agreement with the numerical calculation from Battistin and Iafrati (2003). The peal value obtained in present work is a little larger than that from Battistin and Iafrati (2003), but both of them occur near the spray root of the water jet. Due to the instability of the three-dimensional simulation, the predicted pressure oscillates abound the calculation from Battistin and Iafrati (2003). For the numerical solution, the pressure values are obtained from the virtual pressure sensors placed at the center of the Lagrangian elements. The distance from the pressure sensor to the element may affect the pressure values, as a result, affect the pressure distribution. This is one possible reason for the oscillations of the numerical pressure distribution.

With regard to the total force on the rigid cones, the values of the non-dimensional slamming coefficient are defined as

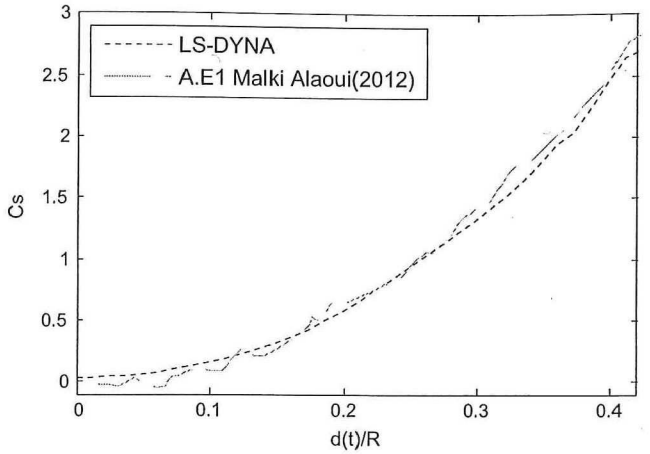

Fig. 34. Non-dimensional impact coefficient for the falling cone with a deadrise angle 30°.

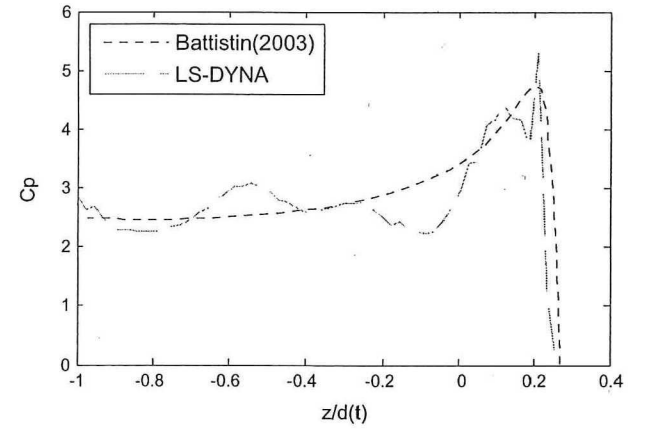

Fig. 35. Non-dimensional pressure distribution on the wetted surface of cone30°.

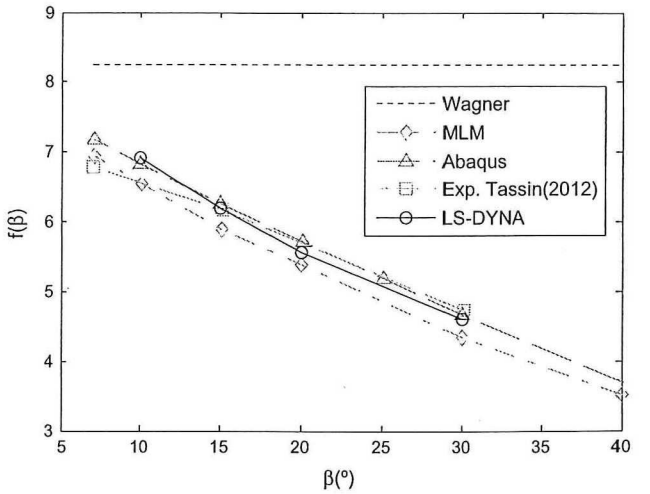

Fig. 36. Non-dimensional slamming coefficients on cones with different deadrise angles.

$f(\beta)=Ftan^3(\beta)/(\rho V^4 t^2)$ in Battistin and Iafrati (2003), where β is the deadrise angle, F the vertical hydrodynamic force, t is the time, V the impact velocity and ρ is the water density. For a cone with a deadrise angle of 30°, Battistin and Iafrati (2003) gave the $f(\beta)$ a value of 4.77, which is in good agreement with the most accurate theoretical prediction, $f(\beta)=4.8$, obtained by Schiffman and Spencer (1951) with a fully theoretical solution for the water impact of a cone with constant velocity. Based on the constant velocity assumption, this value is computed by the present method as, $f(\beta)=4.6$, which is slightly smaller than the numerical and theoretical calculations.

The non-dimensional slamming coefficients on the rigid cones with different deadrise angles are compared with the results from experimental, theoretical and numerical studies, as plotted in Fig. 36. Wagner (1932) theoretically overestimates them, as a result of a higher correction of the wetting factor. For a cone with a small deadrise angle, the present method gives a higher coefficient than the values from other solutions. When the deadrise angle is 15°, the results from LS-DYNA, Abaqus and experiments agree well, while they are larger than the calculations from Modifined Logvinovich Method (MLM). When the deadrise angle is 20° and 30°, LS-DYNA gives smaller values than the results from Abaqus and experiments, but they are still larger than the calculations from Modifined Logvinovich Method (MLM). Generally speaking, the slamming coefficient is larger for the cone with a smaller deadrise angle.

5.4. Pressure distribution and water surface elevation

Figs. 37 and 38 plot the variations of the pressure distribution on the wetted surface of the hemisphere and cone 30°. The non-dimensional penetration $d(t)/R$ denotes the time instant during the impact, while $d(t)/R=0$ means the moment when the structure

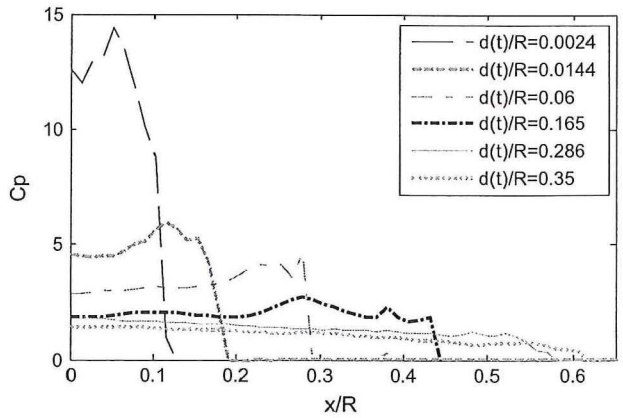

Fig. 37. Variations of the pressure distribution on the wetted surface of the hemisphere.

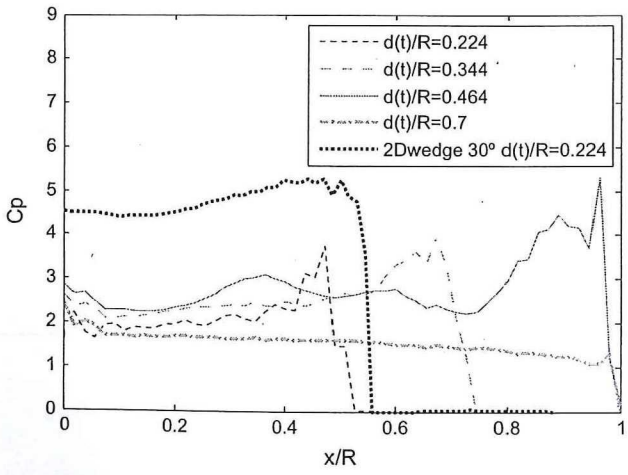

Fig. 38. Variations of the pressure distribution on the wetted surface of the cone 30°.

touches the calm water, and x/R denotes the relative position on the wetted surface. At different time instant, the zero pressure occurs at different position due to the water surface elevation. For the hemisphere, the maximum pressure is located near the spray root of the water surface at the initial stage. As the hemisphere falls, the pressure values drop quickly. The maximum pressure moves towards the lower part of the bottom surface. After $d(t)/R=0.286$, the pressure values do not drop as much as those at the initial stage, as seen in Fig. 37.

As seen in Fig. 38, the maximum pressure on the bottom surface of cone30° is located near the spray root of the water surface, and it increases before the totally immersion of the cone. After the flow separation, the maximum pressure drop quickly and moves to the lower part of the bottom surface. As plotted, the pressure distribution at $d(t)/R=0.224$ on the wetted surface of a 2D wedge with $\beta=30°$ is included as well. The pressure values are larger than the ones on the 3D cone30° due to the three-dimensional effects, however, the peak values almost occur at the same position.

Figs. 39 and 40 show the pressure contours and water surface elevations at different time instants on the hemisphere and the cone30°. It must be noted that only the profiles on x–z plane are presented here, in order to make them visible. The pressure contours correspond to the pressure values which are plotted in Figs. 37 and 38. For the hemisphere, the maximum pressure is located near the intersection between the calm water and the bottom surface when $d(t)/R=0.06$. At the moment of $d(t)/R=0.165$, the pressure values drop greatly and the water jet is produced initially. At the moment of $d(t)/R=0.35$, the water jet departs from the structure surface, and the pressure at the spray root becomes very small. Correspondingly, the impact force decreases after the flow separation as plotted in Fig. 33.

For the cone30°, the maximum pressure is located near the root of the water surface before the totally immersion, as seen in the

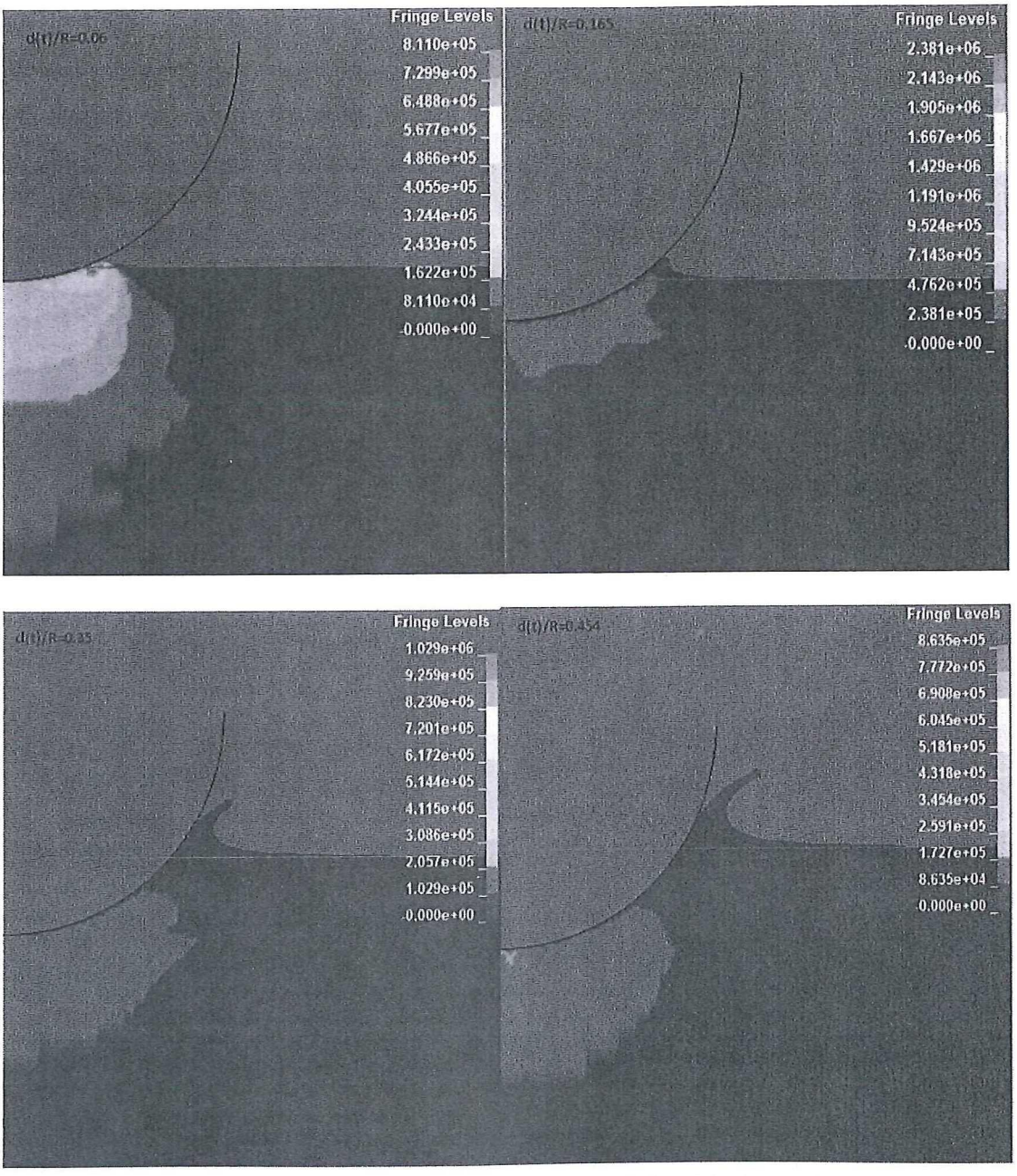

Fig. 39. Pressure contour and water surface elevation on the hemisphere during the water impact.

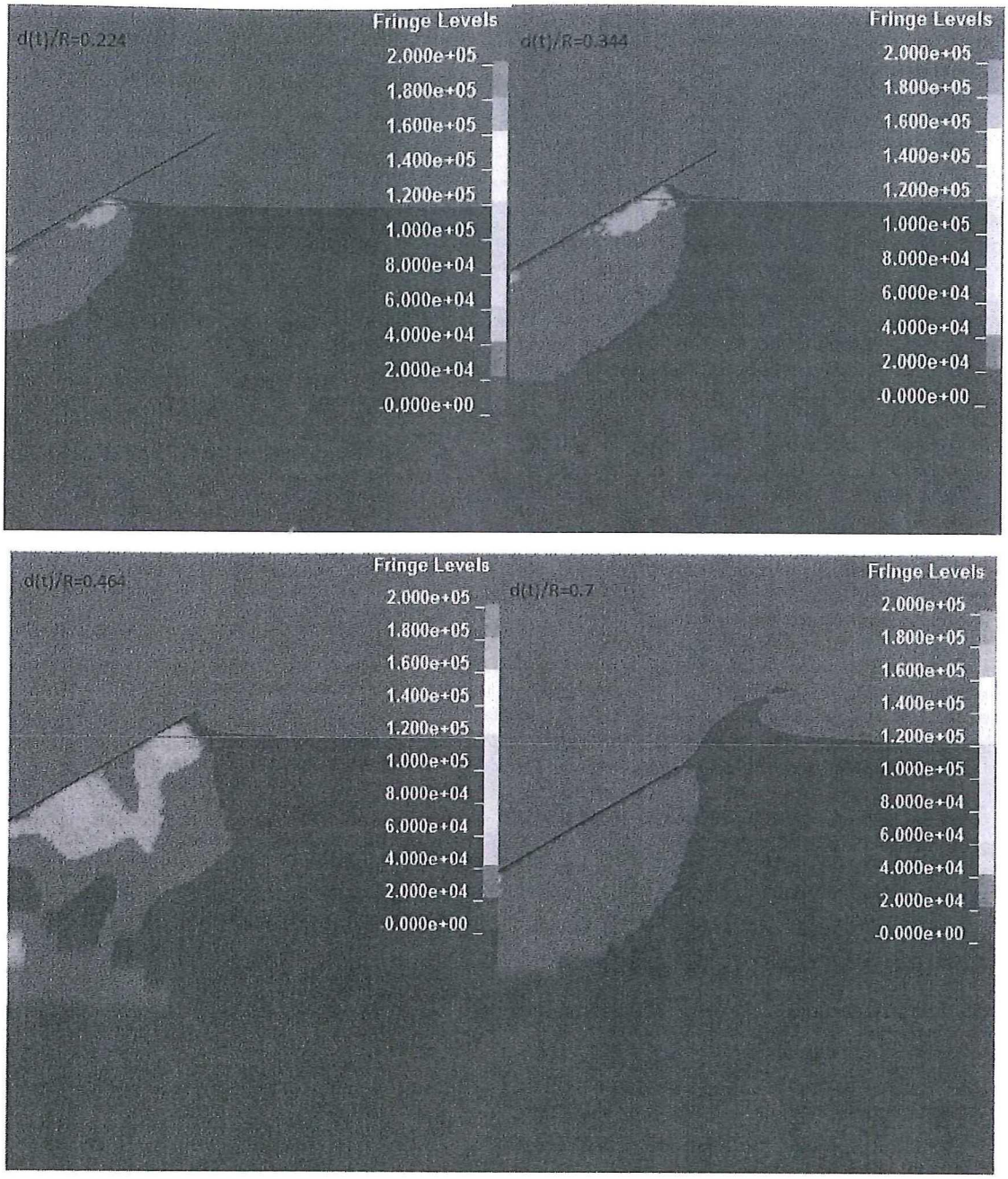

Fig. 40. Pressure contour and water surface elevation on the cone 30° during the water impact.

first two pictures of Fig. 40. When $d(t)/R=0.464$, the cone enters the water completely, and the general maximum pressure occurs at this moment as plotted in Fig. 38. Some numerical noise is observed in the pressure contour at this moment. When $d(t)/R=0.7$, small water droplets departs from the water jet, and the pressure values on the surface become small.

6. Conclusions

In this paper, the water impact of rigid hemisphere and cones with different deadrise angles is numerically investigated, by applying an explicit finite element method based on a multi-material Eulerian formulation and a penalty coupling algorithm. The present work is mainly focused on the application of this method in the water impact problems of 3D bodies.

Firstly, a convergence study was carried out with attention focus on the mesh density of the fluids in the impact domain, contact stiffness and time step. It is found that mesh density is of great importance to the numerical results. Considering the computational efforts, $0.0167R$ mesh size was applied to the models in present work, while the penalty factor is 0.1. The time steps were computed for different cases. For a small mesh size or a high impact velocity, a very small time step is required to make the solution stable, which follows high computational efforts.

Secondly, the numerical calculations were compared with the experimental and analytical results. This is followed by the study on the influence of the constant impact velocity assumption, which showed that the total impact force and the local pressure from the model with constant velocity were larger than the ones from the model with drop velocity, and the differences became large as the structures enter the water. The influence of the

constant velocity assumption can be neglected, only when the initial stage is studied. Then, the time-histories of impact acceleration, velocity, and penetration of the hemisphere, cone20 ° and cone45 ° with drop velocities were compared with available measurements. Some differences were observed in the curves of the acceleration and velocity, probably due to the inaccuracy of the measured velocity in the tests. For the local pressures, the predicted peak values of $P1$ for all the three cases were lower than the measured ones.

For the impact coefficients on the hemisphere with constant velocity, the consistency between the present predictions and the experimental and numerical calculations was satisfactory, though this method underestimated them at the initial stage of the impact. As to the non-dimensional slamming coefficients on cones with different deadrise angles, good agreement was achieved between the present calculations and other results, although some differences were observed.

The pressure contours and water surface elevation of the hemisphere and cone30° during the impact were presented at the last part of this paper, together with the corresponding pressure distributions. It was found that the maximum local pressure occurs when the hemisphere touched calm water, and the total impact force on the cone happened after totally immersion. In conclusion, this method has been properly used to study the 3D water impact problems with good accuracy.

Acknowledgments

The work has been performed in the scope of the project WAVE CONVERTERS- Hydrodynamic analysis of wave energy converters with different motion characteristics, which is financed by the Portuguese Foundation for Science and Technology (FCT) under contract PTDC/EME-MFE/105006/2008.

References

Aquelet, N., Souli, M., Olovsson, L., 2006. Euler–Lagrange coupling with damping effects: Application to slamming problems. Comput. Methods Appl. Mech. Eng. 195, 110–132.

Battistin, D., Iafrati, A., 2003. Hydrodynamic loads during water entry of two-dimensional and axisymmetric bodies. J. Fluids Struct. 17, 643–664.

Chuang, S.L., 1967. Experiments on slamming of wedge-shape bodies. J. Ship Res. 11, 190–198.

Chuang, S.L., Milne, D.T., . Drop tests of cones to investigate the three-dimensional effects of slamming. Naval Ship Research and Development Center, Report 3543.

Dobrovol'skaya, Z.N., 1969. On some problems of similarity flow of fluids with a free surface. J. Fluid Mech. 36, 805–829.

De Backer G., Vantorre M., Victor S., De Rouck J., Beels C., 2008. Investigation of vertical slamming on point absorbers. In: Proceedings of the 27th International Conference Offshore Mechanics Arctic Engineering. (OMAE) Estoril, Portugal, ASME paper no. OMAE2008-57962.

De Backer, G., Vantorre, M., Beels, C., 2009. Experimental investigation of water impact on axisymmetric bodies. Appl. Ocean Res. 31, 143–156.

Estefen S.F., Esperança P.T.T., Ricarte E., Costa P.R., Pinheiro M.M., Clemente C.H., et al., 2008. Experimental and numerical studies of the wave energy hyperbaric device for electricity production. Proceedings of the 27th International Conference Offshore Mechanics Arctic Engineering. (OMAE) Estoril, Portugal, ASME paper no. OMAE2008-57891.

El Malki Alaoui, A., Neme, A., Tassin, A., Jacques, N., 2012. Experimental study of coefficients during vertical water entry of axisymmetric rigid shapes at constant speeds. Appl. Ocean Res. 37, 183–197.

Faltinsen, O.M., Zhao, R., 1997. Water entry of ship sections and axisymmetric bodies. In: Proceedings of the AGARD FDP Workshop on High speed Body Motion in Water. Kiev, Ukraine.

Guedes Soares, C., Bhattacharjee, J., Tello, M., Pietra, L., 2012. Review and classification of wave energy converters. In: Guedes Soares, C., Garbatov, Y., Santos, S. Sutulo T.A. (Eds.), Maritime Engineering and Technology. Taylor & Francis, RINA in UK, pp. 585–594.

Lendenmann, H., Strømsem, K.-C., Dai Pre, M., Arshad, W., Leirbukt, A., Tjensvoll, G., Gulli, T., 2007. Direct generation wave energy converters for optimized electrical power production. In:Proceedings of the 7th European Wave Tidal Energy Conference.

Luo, H.B., Wang, S., Guedes Soares, C., 2011. Numerical prediction of slamming loads on rigid wedge for water entry problem by an explicit finite element method. In: Guedes Soares, C., Fricke, W. (Eds.), Advances in Marine Structures. Taylor & Francis, UK, pp. 41–47

Miloh, T., 1991. On the initial-stage slamming of a rigid sphere in a vertical water entry. Appl. Ocean Res. 13 (1), 8–43.

Marquis, L., Kramer, M., Frigaard, P., 6 October 2010. First power production results from the wave star roshage wave energy converter.In: Proceedings of the 3rd International Conference on Ocean Energy (ICOE 2010), Bilbao.

Nisewanger, C.R., 1996. Experimental determination of pressure distribution on a sphere during water entry. NAVWEPS. Report no. 7808.

Peseux, B., Gornet, L., Donguy, B., 2005. Hydrodynamic impact: numerical and experimental investigations. J. Fluids Struct. 21 (3), 277–303.

Ramos, J., Guedes Soares, C., 1998. Vibratory response of ship hulls to wave impact loads. Int. Shipbuild. Prog. 45 (441), 71–87.

Ramos, J., Incecik, A., Guedes Soares, C., 2000. Experimental study of slam induced stresses in a containership. Mar. Struct. 13 (1), 25–51.

Schiffman, M., Spencer, D.C., 1951. The force of impact on a cone striking a water surface vertical entry. Commun. Pure Appl. Math. 4, 379–417.

Sun, H., Faltinsen, O.M., 2006. Water impact of horizontal circular cylinders and cylindrical shells. Appl. Ocean Res. 28, 299–311.

Stenius, I., Rosn, A., Kuttenkeuler, J., 2006. Explicit FE-modeling of fluid-structure interaction in hull-water impacts. Int. Shipbuild. Prog. 53, 1031–1121.

Silva, D., Rusu, E., Guedes Soares, C., 2013. Evaluation of various technologies for wave energy extraction in the portuguese nearshore. Energies 6, 1344–1364.

von Kármàn, T., 1929. The impact on seaplane floats during landing. National Advisory Committee for Aeronatics. Technical Note no. 321, pp 309–313.

Vantorre, M., Banasiak, R., Verhoeven, R., 2004. Modelling of hydraulic performance and wave energy extraction by a point absorber in heave. Appl. Ocean Res. 26, 6–72.

Wagner, H., 1932. Uber Stossund Gleitvergange an der Oberflache von Flussigkeiten. Z. Angew. Math. Mech. 12, 193–215.

Wang, S., Luo, H.B., Guedes Soares, C., 2012. Explicit FE simulation of slamming load on rigid wedge with various deadrise angles during wate rentry. In: Guedes Soares, C., Garbatov, Y., Sutulo, S., Santos, T.A. (Eds.), Maritime Engineering and Technology, Taylor & Francis, UK, pp. 399–406.

Wang, S., Guedes Soares, C., 2012. Analysis of the water impact of symmetric wedges with a multi-material eulerian formulation. Int. J. Marit. Eng. 154 (PartA4), 191–206.

Wang, S., Luo, H.B. Guedes Soares, C., 2014. Numerical prediction of slamming loads on a bow-flared section during water entry (submitted for publication).

Wang, S., Guedes Soares, C., 2013. Slam induced loads on bow-flared sections with various roll angles. Ocean Eng. 67, 45–57.

Zhao, R., Faltinsen, O.M., 1993. Water entry of two-dimensional bodies. J. Fluid Mech. 246, 593–612.

Zhao, R., Faltinsen, O.M., Aarsnes, J.V., 1996. Water entry of arbitrary two-dimensional sections with and without flow separation. In: Proceedings of the 21st Symposium on Naval Hydrodynamics. pp 408–423.